ACS OMEGA

http://pubs.acs.org/journal/acsodf

Article

Experimental Study to Quantify Fracture Propagation in Hydraulic Fracturing Treatment

Pei He,* Linhua Pan, Zhaohui Lu,* Jiankun Zhou, Chun Meng, and Huawen Yu

Cite This: *ACS Omega* 2022, 7, 27490−27502

Read Online

ACCESS | Metrics & More | Article Recommendations | Supporting Information

ABSTRACT: Hydraulic fracturing plays an important role in the commercial development of unconventional oil and gas, which is directly related to the production of oil and gas wells. An accurate evaluation is critical for hydraulic fracturing, but it is urgent to propose a quantitative assessment of hydraulic fracturing fracture propagation for realizing hydraulic fracturing fracture propagation and multiposition permeability measurement under an in situ stress environment. Herein, a true triaxial stress loading and permeability testing device was designed and fabricated, and a permeability evaluation model was established under various states, which can realize the accurate measurement of multiple faces and the total permeability of tight specimens before and after hydraulic fracturing. It can directly measure permeability under the conditions of the true triaxial fracture propagation experiment. The comparative experimental result shows that the new technique can quantitatively evaluate the fracture propagation experiment of true triaxial hydraulic fracturing. The overall permeability and the directional permeability of the five faces were obtained, and the fracture propagation was evaluated by comparing the change in permeability. The test permeability error rate is within ±10%. Furthermore, a more refined evaluation of hydraulic fracturing fracture propagation can be carried out based on the fracture observation and AE event results. The research results provide a new strategy for a more quantitative and refined evaluation of fracture propagation and help to optimize the parameters of hydraulic fracturing.

1. INTRODUCTION

With the in-depth development of oil and gas exploration and development, unconventional oil and gas resources are becoming more and more critical.[1,2] Hydraulic fracturing technology plays a critical role in commercial development. Therefore, the progress of hydraulic fracturing technology is the critical point of breakthrough in developing unconventional oil and gas resources.[3−6] Optimal implementation has always been the critical direction of hydraulic fracturing technology. The laboratory experiment is an essential means to study this technology. At present, physical experiments of fracture propagation are mainly carried out to simulate field hydraulic fracturing by cracking artificial rock samples or natural rock samples by pumping the fracturing fluid under different environmental conditions. There are many ways to describe the effects of hydraulic fracturing, such as artificial sample description, CT scanning, acoustic emission monitoring, and permeability testing.[7−11] The permeability test under true triaxial stress is a technique to quantitatively evaluate fracture propagation. Permeability often varies in different stress environments. In particular, fracture permeability is extremely sensitive to stress, which is directly related to the production of fractured wells.[12−14] Li et al.[15] studied the permeability anisotropy of sandstone with a size of 2.75 in. × 1.34 in. × 1.34 in. under true triaxial stress and found that the permeability of the sample is sensitive to pressure. However, the experimental apparatus could not be used for the hydraulic fracturing fracture propagation experiment. Liu et al.[16] studied the evolution of the directional permeability of intact and fractured coals. This study obtained permeability only along the loading direction. To obtain permeability in multiple directions, true triaxial stress needs to be loaded and unloaded repeatedly, which is limited to studying the influence of permeability variations under in situ stress. Sato et al.[17] used a Mogi-type true triaxial testing device to investigate permeability anisotropy in two stress directions. The sample size was 2.75 in. × 1.34 in. × 1.34 in. The experimental device could only carry out rock mechanics experiments and not hydraulic fracturing fracture propagation experiments. King et al.[18] developed a multiaxial stress loading system. It can measure fluid permeability and elastic properties for a 2 in. × 2 in. × 2 in. cubic specimen. To achieve sample edge sealing, the sample edge is sealed with silicone rubber. This method had achieved good results in permeability testing. Liu et al.[19] studied

Received: April 22, 2022
Accepted: July 15, 2022
Published: July 26, 2022

Figure 1. True triaxial stress loading and permeability testing integrated module.

permeability variation laws of cylindrical coal specimens under pseudo-triaxial stress, which established a new permeability model based on dual porous elastic theory. However, this device could only be used for axial permeability evaluation. Li et al.[20,21] designed and fabricated a novel multifunctional true triaxial geophysical apparatus that could test specimen permeability and simulate the hydraulic fracturing experiment. Based on the consideration of specimen anisotropy, they established a TTP model that could test the permeability of tight specimens. The new apparatus could only test permeability in one direction of the sample, and the maximum size of the sample could only be 7.87 in. × 7.87 in. × 7.87 in. They revised only the calculation model rather than adopting new methods to improve the permeability testing equipment. The accuracy of the permeability test was worrying. Jiang et al.[22] used the true triaxial geophysical imaging cell of RFDF to measure permeability in three principal directions. The size of the specimen was 3.34 in. × 2.16 in. × 3.34 in. This experimental apparatus could not be used for the hydraulic fracturing test. At present, many instruments can carry out true triaxial mechanics experiments and also can realize various functions. Feng et al.[23] developed a true triaxial apparatus that depended on improving the Mogi-type testing device to achieve true triaxial stress. Frash et al.[24] designed and fabricated a true triaxial device that could simulate multistage hydraulic fracturing of hot dry rocks. Huang et al.[25] developed the laboratory equipment that could only obtain the fracture propagation morphology of hydraulic fracturing under true triaxial stress. To date, a lot of research has been carried out on the permeability model, mainly including the steady-state method and the unsteady-state method. Shi et al.[26,27] derived a permeability model based on the stress effect on the basis of the Gray model when they studied coal rock. It was the S&D model, which was one of the most widely used permeability calculation models. Seidle et al.[28] proposed a new permeability calculation model based on the permeability change caused by matrix deformation of coal rock compression. Connell et al.[29] presented permeability calculation models under various boundary conditions. In summary, we find that the existing research studies mainly have the following shortcomings:

(1) The versatility of specimen size and permeability testing is limited. Under true triaxial stress, the experimental apparatus that can carry out the fracture propagation experiment and the permeability test at the same time is mainly for small-size samples.[20,21] Specimens with sizes of 11.81 in. × 1.81 in. × 11.81 in. and above cannot realize these two functions simultaneously, and the permeability test of the large-scale experimental specimen is insufficient. The existing small-size apparatus can only carry out a one-way permeability test and not multiple faces and total permeability test of the sample.
(2) The permeability testing apparatus does not meet the permeability testing requirements of tight specimens. The experimental equipment that can carry out hydraulic fracturing fracture propagation experiments is mainly based on conventional permeability testing equipment. For tight specimens, only the optimized calculation model is used to obtain permeability, which has low testing accuracy and no substantial improvement from the source and principle of the apparatus.
(3) The existing permeability model cannot meet the needs. The current permeability models are mainly the steady-state method and the unsteady-state method.[30−32] However, the steady-state method is mainly used for the permeability of large-size samples under true triaxial stress, which cannot meet the needs of the test accuracy of tight specimens. It also cannot meet the test requirement of multiple faces and total permeability in the developed experimental apparatus.

In this study, based on the analysis of problems in the same current apparatus and test model, we design and fabricate the true triaxial stress loading and permeability integration module of large-size specimens and improve the sealing parts and structures of the experimental sample. It builds the new

https://doi.org/10.1021/acsomega.2c02517
ACS Omega 2022, 7, 27490−27502

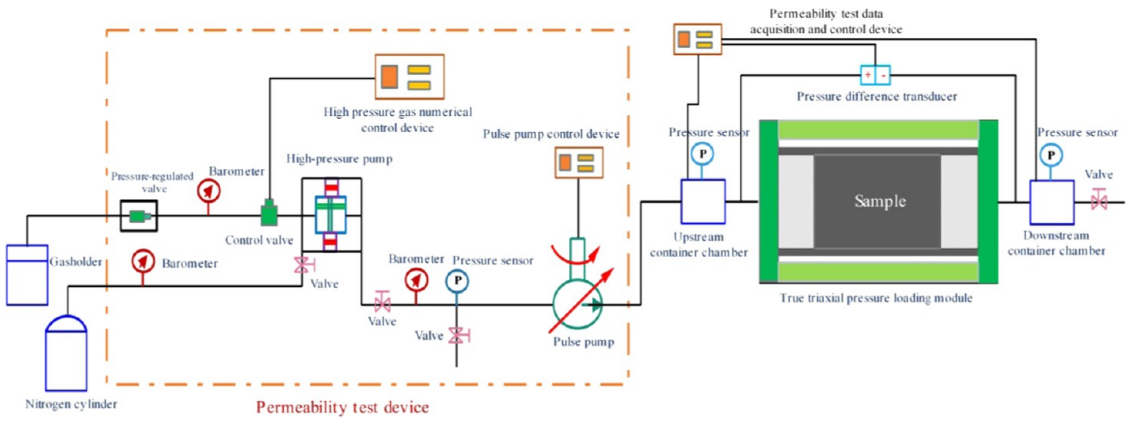

Figure 2. Permeability test flow chart.

permeability testing equipment and establishes models of different faces and total permeability before and after hydraulic fracturing. Multiple faces and general permeability tests of tight specimens are realized. Through comparison experiments, it is verified that the equipment and method have good compatibility, and the error rate meets the relevant requirements. This provides a new way to quantitatively evaluate the fracture propagation of true triaxial hydraulic fracturing.

2. DEVELOPMENT OF THE EXPERIMENTAL INSTRUMENT AND METHOD

To solve the sample permeability test problem, with a size of 11.81 in. × 11.81 in. × 11.81 in., we design experimental devices and establish experimental methods. This achieves the objective of quantitative evaluation of the true triaxial hydraulic fracturing fracture propagation experiment under an in situ stress environment.

2.1. Experimental Instrument Design. *2.1.1. True triaxial stress loading and permeability testing integrated module.* To carry out the permeability test before and after fracturing without reloading and unloading the environmental stress in true triaxial stress, we need to improve the total module of the true triaxial stress loading and permeability test as follows (Figure 1).

(1) Loading true triaxial stress: Five 11.81 in. × 11.81 in. × 11.81 in. steel base plates are installed on five different faces of the experimental specimen except for the fracturing wellbore direction (Figure S1). The stepped-shaped holes (Figures S3 and S4) help to collect the test gas in the center of each plate. They are sealed with thread and a rubber gasket. Three grooves of different lengths are opened on the base plate surface, which are used to embed acoustic emission sensor acquisition lines and permeability test steel pipelines. In addition, the 11.81 in. long groove (Figure S2) is opened on the 1.18 in. broad face of each base plate, which is used to pass permeability test pipelines under loading true triaxial stress.

(2) Collecting gas pipelines: To collect the permeability test gas of different faces, a test gas pipeline managing and switching device is arranged in the wellbore direction, which can independently switch on and off the gas collection pipelines at different faces of the experimental specimen and achieve gas metering for each face and the testing specimen.

(3) Sealed experimental specimen: In the experiment, 12 edges of the cube specimen are exposed outside steel base plates, and the purpose of sealing gas cannot be achieved by relying solely on the plate and true triaxial stress. We use the core sleeve to wrap the experimental specimen and seal the 12 edges by true triaxial stress (Figure S5).

(4) Sealed wellbore: The wellbore is the channel for pumping the fracturing fluid and permeability test gas. A high degree of adhesion is required between the wellbore and the testing specimen. We use a special structure of the wellbore (Figure S6) and epoxy resin to seal the small gap between the wellbore and the experimental specimen, achieving a better result.

2.1.2. Permeability test module. Because most experimental specimens are tight samples before the hydraulic fracturing experiment, conventional permeability testing methods cannot achieve the purpose of permeability testing. They require other ways to accomplish this. We use the pulse attenuation method to test permeability before the hydraulic fracturing experiment and make the following improvements to the permeability test module (Figure 2)

(1) Permeability testing device (Figure S7): It mainly consists of a gas pressurization device (a booster pump, an air compressor, and a gas storage tank), a balance vessel, a pulse generation device, etc. The gas pressurization device can provide a stable permeability test gas with a maximum pressure of 20 MPa. The pulse generation device can cut off the high-pressure gas at a fixed frequency to generate a regular pulse gas that meets the requirements. The balance vessel is composed of two constant volume cavities, and the pressure of upstream and downstream container chambers is collected in real time.

(2) Permeability test data acquisition and control: Two of the critical factors of the permeability test are the pressure and the pressure difference. The maximum test pressure of upstream and downstream container chamber pressure sensors is 20 MPa, and the error is less than 0.03%. The minimum differential pressure of the differential pressure sensor can reach 10 kPa, and the differential pressure is less than 0.05%. The theoretical test accuracy is 0.000001 mD. Data acquisition is controlled by self-programmed software (Figure S8).

https://doi.org/10.1021/acsomega.2c02517
ACS Omega 2022, 7, 27490−27502

2.2. Experimental Method. The permeability of the experimental specimen changes greatly before and after the hydraulic fracturing experiment, and there are significant differences in the requirements of permeability test methods. In addition, there are some differences in the total permeability and single-face permeability of the experimental specimen due to different test gas seepage methods.

2.2.1. Permeability model before the hydraulic fracturing experiment. 2.2.1.1. Total Permeability. According to Darcy's law and the law of conservation of mass[33]

$$q = -\frac{KA}{\mu}\frac{\partial P}{\partial x} \tag{1}$$

$$q_n = \rho q = -\frac{KA\rho}{\mu}\frac{\partial P}{\partial x} \tag{2}$$

where q is the gas volume flow, P is the pressure in the x-direction, K is the permeability of the specimen, A is the specimen area, μ is the viscosity, q_n is the gas molar flow, and ρ is the density.

In the X-axis direction of the specimen, the net increase of volume flow $\mathrm{d}q_n$ per unit time $\mathrm{d}t$ through the unit distance $\mathrm{d}x$ is as follows

$$\mathrm{d}q_n = -\frac{\partial}{\partial x}\left(\frac{KA\rho}{\mu}\frac{\partial P}{\partial x}\right)\mathrm{d}x\mathrm{d}t \tag{3}$$

Due to the compressibility of the gas and the pores of the specimen, the net increase of volume flow occurs in the volume element per unit length distance $\mathrm{d}x$. Then, the total increase of gas mass per unit time $\mathrm{d}t$ is

$$\mathrm{d}q_n = \rho\frac{\partial}{\partial t}(V_\mathrm{p}\mathrm{d}x/L)\mathrm{d}t + (V_\mathrm{p}\mathrm{d}x/L)\frac{\partial \rho}{\partial t}\mathrm{d}t \tag{4}$$

where V_p is the pore volume of the specimen. The first term is the gas mass increase caused by the compressibility of the specimen pore, and the second term is the gas mass increase generated by gas compressibility. Formulas 3 and 4 can further obtain

$$\frac{\partial}{\partial x}\left(\frac{KA}{\mu}\frac{\partial P}{\partial x}\right)\mathrm{d}x\mathrm{d}t = \rho\frac{\partial}{\partial t}(V_\mathrm{p}\mathrm{d}x/L)\mathrm{d}t + (V_\mathrm{p}\mathrm{d}x/L)\frac{\partial \rho}{\partial t}\mathrm{d}t \tag{5}$$

Assuming that gas viscosity and permeability are constant, formula 5 can be simplified as

$$\frac{\partial^2 P}{\partial x^2} = \frac{\mu}{K}\left(\frac{\partial \varphi}{\partial t} + \varphi\beta\frac{\partial P}{\partial t}\right) - \beta\left(\frac{\partial P}{\partial x}\right)^2 \tag{6}$$

where β is the gas compression coefficient, which is calculated as follows

$$\beta = -\frac{1}{\nu}\left(\frac{\partial V}{\partial P}\right)_T = \frac{1}{\rho}\left(\frac{\partial \rho}{\partial P}\right) = \frac{1}{P} - \frac{1}{Z}\left(\frac{\partial Z}{\partial P}\right)_T \tag{7}$$

where V is the volume, ϕ is the porosity of the experimental specimen, T is the temperature, and Z is the compression factor. The calculation formula is as follows

$$\phi = \frac{V_\mathrm{p}}{V} = \frac{V_\mathrm{p}}{AL} \tag{8}$$

For tight rocks, the porosity is microscopic and the pore volume changes very little with pressure and time. Therefore, the first term on the right of formula 6 can be ignored. Then, formula 6 can be simplified as

$$\frac{\partial^2 P}{\partial x^2} = -\beta\left(\frac{\partial P}{\partial x}\right)^2 \tag{9}$$

The pressure distribution in the specimen has no relationship with time in the early stage. However, when the pressure changes significantly, the gas compression coefficient β is not constant. The compression factor Z is 1 for an ideal gas. Formula 7 can be simplified as

$$\beta = \frac{1}{P} \tag{10}$$

Further, formula 9 can be simplified as

$$\frac{\partial^2 P}{\partial x^2} + \frac{1}{P}\left(\frac{\partial P}{\partial x}\right)^2 = \frac{\partial}{\partial x}\left(P\frac{\partial P}{\partial x}\right) = 0 \tag{11}$$

According to formula 11, the pressure distribution in the specimen is a function of the gas pressure and distance in the upstream and downstream container chambers

$$P^2 = \frac{P_\mathrm{u}^2 - P_\mathrm{d}^2}{L}x + P_\mathrm{d}^2 \tag{12}$$

where P_u is the upstream container chamber pressure and P_d is the downstream container chamber pressure.

$$\frac{\partial P}{\partial x} = \frac{P_\mathrm{u}^2 - P_\mathrm{d}^2}{2LP} \tag{13}$$

When the gas compression coefficient β is considered to be a constant within a small pressure variation range, formula 9 can be simplified as

$$\frac{\partial^2 P}{\partial x^2} = 0 \tag{14}$$

Then, the relationship between pressure and pressure change with distance x is

$$P = \frac{P_\mathrm{u} - P_\mathrm{d}}{L}x + P_\mathrm{d} \tag{15}$$

$$\frac{\partial P}{\partial x} = \frac{P_\mathrm{u} - P_\mathrm{d}}{L} \tag{16}$$

It can be seen from formulas 12 and 15 that the pressure distribution in the specimen is the parameter of equilibrium pressure for an ideal gas.

The volume flow in the gas container chamber is

$$q = \frac{V}{\rho}\frac{\mathrm{d}p}{\mathrm{d}t} = V\beta\frac{\mathrm{d}P}{\mathrm{d}t} = V\frac{1}{P}\frac{\mathrm{d}P}{\mathrm{d}t} \tag{17}$$

Based on the direction of fluid flow, formulas 13 and 17 can be established by the upstream and downstream container chamber pressures

$$V_\mathrm{u}\frac{1}{P_\mathrm{u}}\frac{\mathrm{d}P_\mathrm{u}}{\mathrm{d}t} = -\frac{KA}{\mu}\frac{(P_\mathrm{u}^2 - P_\mathrm{d}^2)}{2LP_\mathrm{u}} \tag{18}$$

$$V_\mathrm{d}\frac{1}{P_\mathrm{d}}\frac{\mathrm{d}P_\mathrm{d}}{\mathrm{d}t} = -\frac{KA}{\mu}\frac{(P_\mathrm{u}^2 - P_\mathrm{d}^2)}{2LP_\mathrm{d}} \tag{19}$$

https://doi.org/10.1021/acsomega.2c02517
ACS Omega 2022, 7, 27490−27502

where V_u is the upstream container chamber volume and V_d is the downstream container chamber volume. Then, formulas 18 and 19 can be simplified as

$$V_u \frac{dP_u}{dt} = -\frac{KA}{\mu}\frac{(P_u^2 - P_d^2)}{2L} \tag{20}$$

$$V_d \frac{dP_d}{dt} = -\frac{KA}{\mu}\frac{(P_u^2 - P_d^2)}{2L} \tag{21}$$

By combining formulas 20 and 21, we obtain

$$V_d \frac{dP_d}{dt} = V_u \frac{dP_u}{dt} \tag{22}$$

When $V_u = V_d$, it can be seen from formula 22 that the pressure increase in the upstream container chamber is equal to the pressure decrease in the downstream container chamber, and we obtain

$$P_d + P_u = P_{u,0} - dP_u + P_{d,0} + dP_d = P_{u,0} + P_{d,0} \tag{23}$$

where $P_{u,0}$ is the initial pressure in the upstream container chamber and $P_{d,0}$ is the initial pressure in the downstream container chamber.

By subtracting formula 21 from formula 20, we obtain

$$\begin{aligned}\frac{d(P_u - P_d)}{dt} &= -\frac{KA}{\mu}\left(\frac{1}{V_u} + \frac{1}{V_d}\right)\frac{(P_u^2 - P_d^2)}{2L} \\ &= -\frac{KA}{\mu}\left(\frac{1}{V_u} + \frac{1}{V_d}\right)\frac{(P_u + P_d)(P_u - P_d)}{2L}\end{aligned} \tag{24}$$

By combining formulas 23 and 24, we obtain

$$\frac{d(P_u - P_d)}{dt} = -\frac{KA}{\mu L}\left(\frac{1}{V_u} + \frac{1}{V_d}\right)\frac{(P_{u,0} + P_{d,0})}{2L}(P_u - P_d) \tag{25}$$

Formula 25 can be integrated as

$$\frac{(P_u - P_d)}{(P_{u,0} - P_{d,0})} = e^{-\alpha t} \tag{26}$$

$$\alpha = \frac{KA(P_{u,0} + P_{d,0})}{2\mu L}\left(\frac{1}{V_u} + \frac{1}{V_d}\right) \tag{27}$$

Formulas 26 and 27 are used for calculating the permeability of experimental specimens tested by the ideal gas pulse attenuation method. For a nonideal gas, the gas compression factor is Z and the gas compression coefficient is

$$\beta = \frac{Z}{P} \tag{28}$$

Then, formula 27 can be changed to

$$\alpha = \frac{ZKA}{\beta\mu L}\left(\frac{1}{V_u} + \frac{1}{V_d}\right) \tag{29}$$

It is considered that the compressibility coefficients of pressure gas β in the upstream and downstream container chambers are the same. We transform formula 26 and combine it with formula 29 to obtain

$$\begin{cases} K = \dfrac{\beta\alpha\mu L}{2A\left(\frac{1}{V_u} + \frac{1}{V_d}\right)} \\ \alpha = \dfrac{1}{t}\ln\dfrac{(P_{u,0} - P_{d,0})}{(P_u - P_d)} \end{cases} \tag{30}$$

where K is the total permeability, A is the specimen section area, β is the gas compression coefficient, L is the specimen length, α is the fitting value, and t is the test time.

Further, combined with the characteristics of gas flow tested in the experimental device (Figure S9), the total permeability test is radial flow, which satisfies formula 31

$$q = \frac{2\pi K h(P_e - P_{wf})}{\mu \ln\frac{r_e}{r_w}} \tag{31}$$

where q is the gas flow, h is the seepage thickness of the specimen, $P_e - P_{wf}$ is the flow pressure difference, r_e is the outer circle radius of the sample, and r_w is the outer diameter of the wellbore.

From formula 30, the volumes of the upstream and downstream containers each are 1000 mL in the experimental device, i.e., V_u and V_d each are equal to 1000 mL. Therefore, the calculation model of the total permeability of the experimental specimen before hydraulic fracturing can be expressed as

$$\begin{cases} K = \dfrac{125\beta\alpha\mu r_e}{\pi r_w h_2} \\ \alpha = \dfrac{1}{t}\ln\dfrac{(P_{u,0} - P_{d,0})}{(P_u - P_d)} \end{cases} \tag{32}$$

where h_2 is the perforation length or open hole section length.

2.2.1.2. Single-Face Permeability. According to the calculation model of pulse attenuation test permeability, the single-face permeability test of the experimental specimen meets the one-dimensional seepage characteristics, which is similar to the pulse attenuation test law of cylindrical cores. Therefore, according to formula 30, permeability calculation models of four single faces that are parallel to the fractured wellbore in the experimental specimen (Figure S9) can establish

$$\begin{cases} K = \dfrac{250\beta\alpha\mu}{h_2} \\ \alpha = \dfrac{1}{t}\ln\dfrac{(P_{u,0} - P_{d,0})}{(P_u - P_d)} \end{cases} \tag{33}$$

Due to different seepage areas on the experimental specimen face perpendicular to the experimental wellbore (Figure S9), combined with formula 30, formula 33 can be expressed as

$$\begin{cases} K = \dfrac{250\beta\alpha\mu(H - h_1 - h_2)}{H^2} \\ \alpha = \dfrac{1}{t}\ln\dfrac{(P_{u,0} - P_{d,0})}{(P_u - P_d)} \end{cases} \tag{34}$$

where H is the width of the specimen and h_1 is the length of the fracturing wellbore.

https://doi.org/10.1021/acsomega.2c02517
ACS Omega 2022, 7, 27490−27502

Table 1. Experimental Scheme for Fracture Propagation and Permeability Test of True Triaxial Hydraulic Fracturing

name		gas pressure (MPa)		X-direction pressure (MPa)		Y-direction pressure (MPa)		Z-direction pressure (MPa)		note
		sample 1#	sample 2#	sample 1#	sample 2#	sample 1#	sample 2#	sample 1#	sample 2#	
permeability before the hydraulic fracturing experiment	Total	4.5	10.5	9	20	7	15	12	25	
	Face 1	4.5	10.5	9	20	7	15	12	25	
	Face 2	4.5	10.5	9	20	7	15	12	25	
	Face 3	4.5	10.5	9	20	7	15	12	25	
	Face 4	4.5	10.5	9	20	7	15	12	25	
	Face 5	4.5	10.5	9	20	7	15	12	25	perpendicular to the wellbore
hydraulic fracturing experiment			9	20	7	15	12	25		
permeability after the hydraulic fracturing experiment	Total	1	1	9	20	7	15	12	25	
	Face 1	1	1	9	20	7	15	12	25	
	Face 2	1	1	9	20	7	15	12	25	
	Face 3	1	1	9	20	7	15	12	25	
	Face 4	1	1	9	20	7	15	12	25	
	Face 5	1	1	9	20	7	15	12	25	perpendicular to the wellbore
permeability of the small cylindrical sample	Face 1	4.5	10.5	9	20	9	20	9	20	the size is Φ1 in. × H 2 in.
	Face 2	4.5	10.5	9	20	9	20	9	20	
	Face 3	4.5	10.5	9	20	9	20	9	20	
	Face 4	4.5	10.5	9	20	9	20	9	20	
	Face 5	4.5	10.5	9	20	9	20	9	20	

In short, formula 33 is the four-single-face permeability calculation model, which is parallel to the fractured wellbore, and formula 34 is the bottom-face permeability calculation model perpendicular to the fractured wellbore.

2.2.2. Permeability model after the hydraulic fracturing experiment. In the hydraulic fracturing experiment, many artificial fractures are produced in the sample. The permeability of the experimental sample often increases by several orders of magnitude. The permeability model established before the hydraulic fracturing experiment cannot meet the needs. A post-fracturing permeability testing model is established based on conventional permeability testing methods.

2.2.2.1. Total Permeability. After the hydraulic fracturing experiment, many artificial fractures are generated, and the permeability of the experimental specimen is the sum of fracture permeability K_f and matrix permeability K_m.[34,35] If $K_f \gg K_m$ in the actual flow process, the matrix permeability can be ignored. That is, $K = K_f + K_m \approx K_f$.

According to the Boussinesq equation,[36] the flow through the crack per unit length is

$$q_1 = \frac{b^3}{12\mu}\frac{dp}{dx} \tag{35}$$

where q_1 is the gas flow of fracture, b is the fracture width, μ is the gas viscosity, and $\frac{dp}{dx}$ is the pressure gradient.

When the total fracture length is L, the full flow through the rock seepage area is

$$Q = Lq_1 = \frac{Lb^3}{12\mu}\frac{dp}{dx} \tag{36}$$

As Φ_f is the fracture porosity, which is $\Phi_f = \frac{Lb}{A}$, formula 36 can be expressed as

$$Q = \frac{A\Phi_f b^2}{12\mu}\frac{dp}{dx} \tag{37}$$

The rock fracture permeability is K_f. According to Darcy's law,

$$Q = \frac{2\pi h_2 K_f}{\mu \ln\frac{r_e}{r_w}}\frac{dp}{dx} \tag{38}$$

According to the principle of equivalent permeability resistance, formulas 37 and 39 can be expressed as

$$K_f = \frac{LQ \ln\frac{r_e}{r_w}}{24\pi\mu h_2 \Delta p} \tag{39}$$

Under the experimental conditions, the crack width b can be obtained by actual measurement, and the total crack length L can be approximately expressed as $H/2$. The total permeability of the experimental specimen after the hydraulic fracturing experiment can be described as follows

$$K \approx K_f = \frac{HQ \ln\frac{r_e}{r_w}}{48\pi\mu h_2 \Delta p} \tag{40}$$

where K is the total permeability of the sample, H is the width of the specimen, h_2 is the perforation length or open hole section length, Q is the gas flow, r_e is the outer circle radius of the specimen, r_w is the outer diameter of the wellbore, Δp is the gas pressure difference, and μ is the gas viscosity.

2.2.2.2. Single-Face Permeability. After the hydraulic fracturing fracture propagation experiment is completed, the single-face permeability test of the experimental specimen is carried out, which can be divided into two situations: the first situation is that there is no fracture on the face. The permeability of this face will continue to maintain the original state, which can be judged by no gas flow, minimal flow, or no flow differential pressure. We can use prehydraulic fracture permeability as the post-hydraulic fracture permeability. The

https://doi.org/10.1021/acsomega.2c02517
ACS Omega 2022, 7, 27490−27502

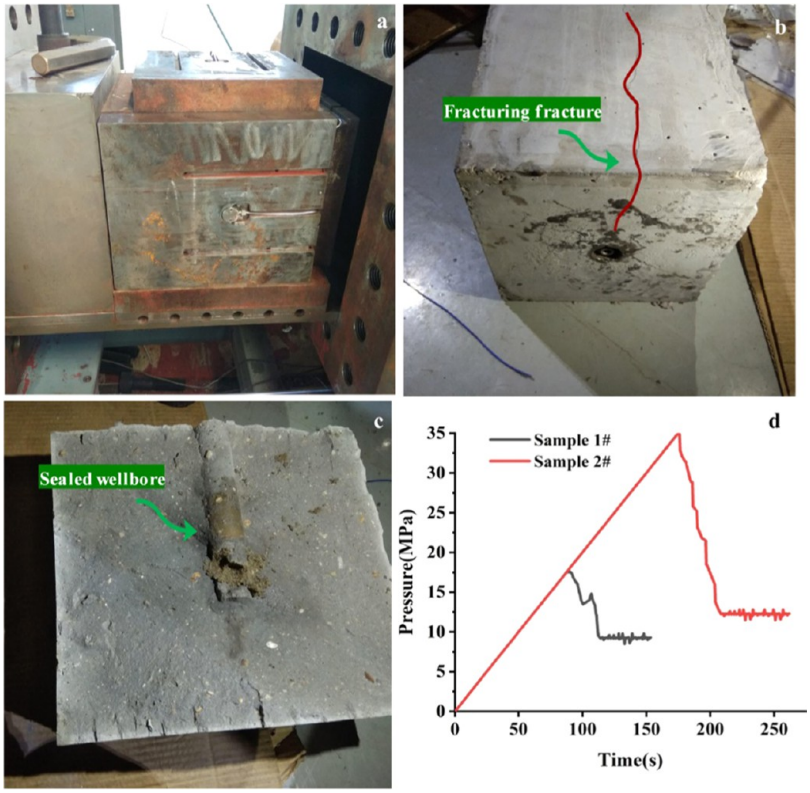

Figure 3. Hydraulic fracturing experiment: (a) package sample, (b) sample after hydraulic fracturing, (c) sample cut, and (d) experimental pressure curves.

second situation is that there are fractures on the face. A gas permeability test is required to obtain the permeability.

Due to cracks in the experimental specimen, its flow state does not entirely conform to Darcy's law. Darcy's formula needs to be corrected. The four-single-face permeability calculation model parallel to the fractured wellbore in the experimental specimen (Figure S9) can be expressed as follows

$$K = \frac{\mu QLA}{A^2\Delta P - \varepsilon\rho Q^2 L} = \frac{2\pi\mu QHh_2}{8\pi^2 h_2^2\Delta P - \varepsilon\rho Q^2 H} \quad (41)$$

Due to different seepage areas of the bottom face perpendicular to the wellbore (Figure S9), the calculation model of bottom-face permeability is expressed as

$$K = \frac{\mu QHh_2(H - h_1 - h_2)}{H^4\Delta P - \varepsilon\rho Q^2(H - h_1 - h_2)} \quad (42)$$

where ε is the pore characteristic parameter of the experimental sample and h_1 is the length of the fracturing wellbore.

3. EXPERIMENTAL SCHEME

To verify the experimental instruments and methods, two groups of experiments were carried out under different conditions (Table 1): the total permeability of the experimental sample, single-face permeability, and the permeability of the contrast testing samples (small cylindrical samples drilled from the experimental specimen). Furthermore, the fracture propagation characteristics and acoustic emission monitoring results of testing samples were combined to verify the impacts of hydraulic fracturing. To verify the sealing effect of the experimental equipment, two different true triaxial stresses of low pressure and middle−high pressure were adopted. Two schemes of 3.5−4.5 and 9.5−10.5 MPa were used for the permeability pulse gas pressure before the hydraulic fracturing experiment. The permeability of small cylindrical samples was measured by a mature pulse permeability testing method. Their confining pressures were 9 and 20 MPa, respectively. To simulate tight samples and meet the needs of regular edges of the experimental specimen, the experimental specimens were molded and poured with cement and sand (Figures S10 and S11). The sample size was 11.81 in. × 11.81 in. × 11.81 in. The hydraulic loading rate of the fracturing fluid was increased by 0.2 MPa/s until the experimental specimen was damaged by hydraulic fracturing (Figure 3).

4. RESULTS AND DISCUSSION

The permeability and fracture propagation before and after hydraulic fracturing are discussed and analyzed using the developed experimental instrument and methods. The effectiveness of the new technique was verified by comparing experiments, generated fracture descriptions, and acoustic emission event monitoring.

4.1. Before the Hydraulic Fracturing Experiment. *4.1.1. Experiment with the new technique.* Before the hydraulic fracturing, we used the new technique to test the permeability of samples 1# and 2# (Total, Face 1, 2, 3, 4 and 5). Gas pressure−time curves are shown in Figures 4 and 5. Experimental environmental conditions are listed in Table 1. The experimental results are shown in Table 2. It is observed that the experimental instrument has good sealing performance under low pressure (3.5−4.5 MPa) and medium−high pressure (9.5−10.5 MPa). The pulse gas pressure in the

https://doi.org/10.1021/acsomega.2c02517
ACS Omega 2022, 7, 27490−27502

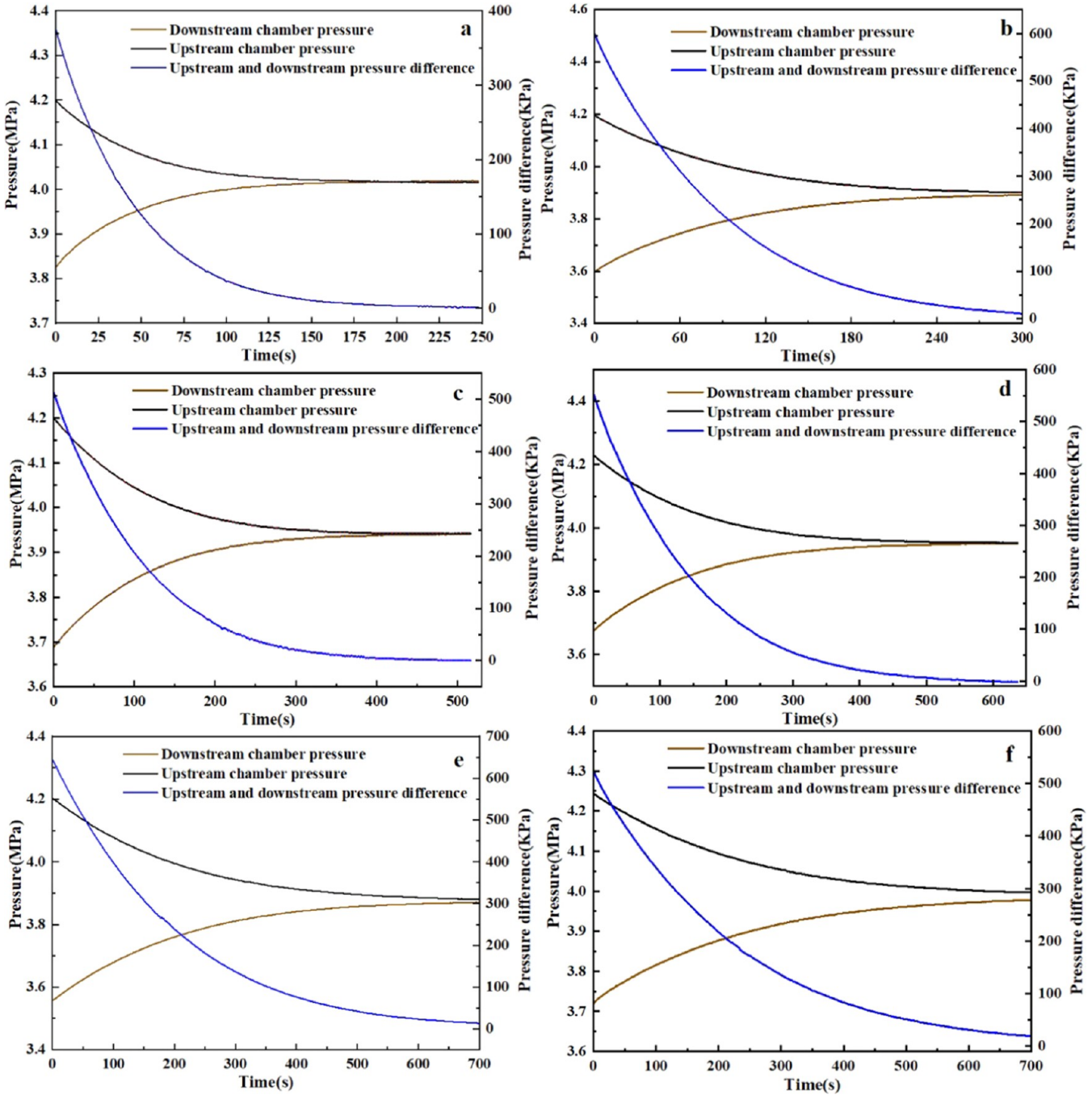

Figure 4. Gas pressure−time curves of sample 1#: (a) Total, (b) Face 1, (c) Face 2, (d) Face 3, (e) Face 4, and (f) Face 5.

upstream and downstream container chambers changes steadily and slowly. The gas pressure in the upstream container chamber can steadily decay and penetrate through the specimen into the downstream container chamber to complete the pulse attenuation test. Under the conditions of low true triaxial stress and low gas pressure, the pressure balance of the upstream and downstream container chambers is achieved in approximately 10 min to complete the experiment. Under the medium−high true triaxial stress and medium−high gas pressure, more than 1 h is required to achieve the gas pressure balance in the upstream and downstream container chambers. The experiment time greatly increases. It can be observed that the increase of true triaxial stress and pulse gas pressure will significantly prolong the gas pressure balance time and experiment time. In the experiment on the pulse permeability of small cylindrical samples, it is found that gas cannot penetrate tight samples under low pressure. The gas pressure in the upstream and downstream container chambers is almost unchanged, making permeability testing unsuccessful. Therefore, higher and more stable gas pressure is favorable for permeability testing. Of course, higher gas pressure also puts forward higher requirements for specimen sealing and prolongs the experiment time. A longer time is required for high-pressure gas to achieve a pressure balance between upstream and downstream in the process of permeating the specimen. Medium−low (4−8 MPa) gas pressure is recommended for smooth and rapid permeability tests.

https://doi.org/10.1021/acsomega.2c02517
ACS Omega 2022, 7, 27490−27502

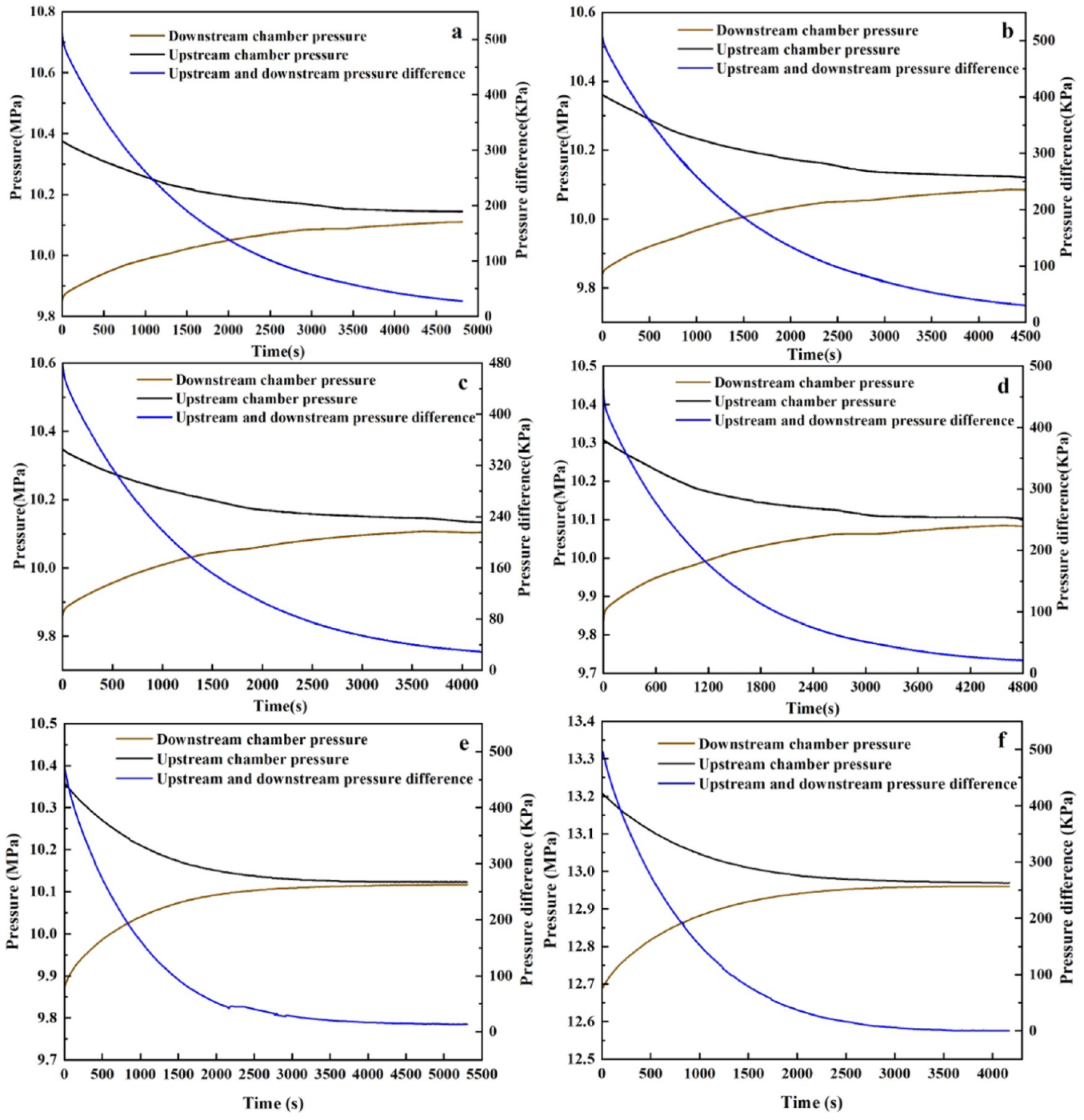

Figure 5. Gas pressure−time curves of sample 2#: (a) Total, (b) Face 1, (c) Face 2, (d) Face 3, (e) Face 4, and (f) Face 5.

Table 2. Permeability of Samples 1# and 2# on Different Faces and Drilled Small Cylindrical Samples before and after Hydraulic Fracturing

	sample 1# permeability (mD)			sample 2# permeability (mD)		
name	before hydraulic fracturing	after hydraulic fracturing	small cylindrical sample	before hydraulic fracturing	after hydraulic fracturing	small cylindrical sample
Face 1	0.004535	952.56	0.004884	0.006238	560.26	0.005871
Face 2	0.007363	743.76	0.007563	0.002128		0.001936
Face 3	0.006080		0.005860	0.002150	448.62	0.002210
Face 4	0.004787		0.004523	0.004522	280.49	0.004314
Face 5	0.004432	845.65	0.004166	0.006280		0.006956
Total	0.007189	1009.21		0.006820	662.45	

https://doi.org/10.1021/acsomega.2c02517
ACS Omega 2022, 7, 27490−27502

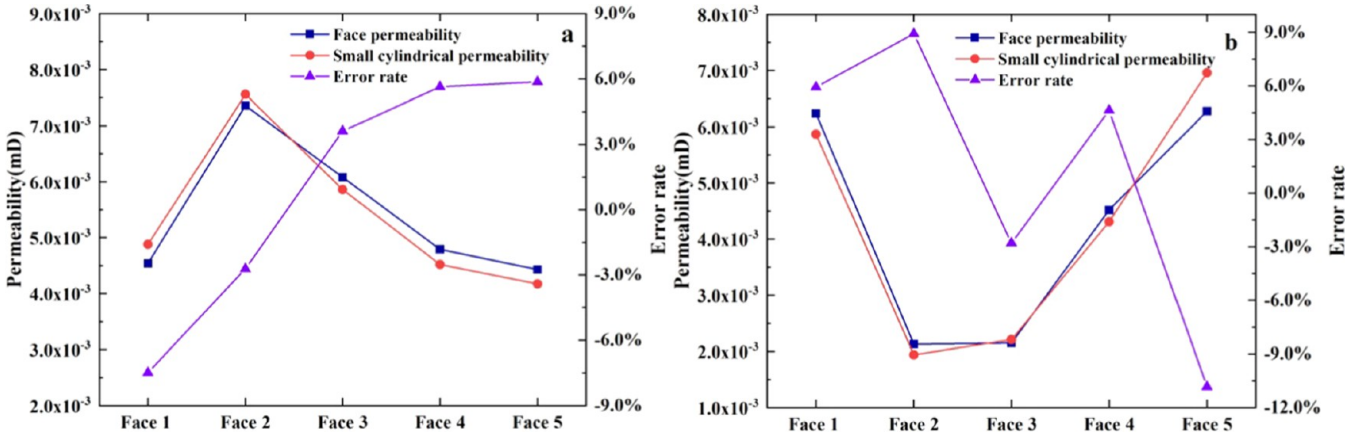

Figure 6. Permeability comparison between the face and the small cylinder: (a) sample 1# and (b) sample 2#.

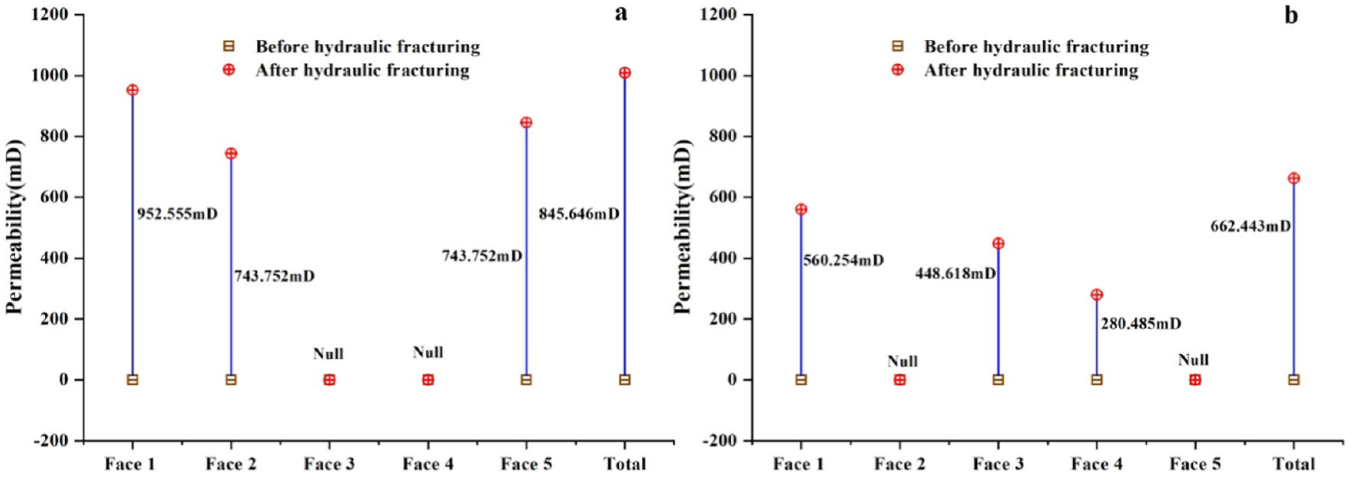

Figure 7. Comparison of permeability before and after the hydraulic fracturing experiment: (a) sample 1# and (b) sample 2#.

4.1.2. Experimental comparison. We drilled 10 small cylindrical samples of Φ1 in. × H 2 in. from five different faces of samples 1# and 2#, and permeability was tested by the pulse attenuation method. The experimental results are shown in Table 2. The permeability of the small cylinder of sample 1# is 0.004166−0.007563 mD, and the face permeability is 0.004432−0.007363 mD. The error rate is −7.15−6.39%. The permeability of the small cylinder of sample 2# is 0.001936−0.006956 mD, and the face permeability is 0.002128−0.006280 mD. The error rate is −9.72−9.92%. It can be seen that the error rate of the two samples is within ±10%. Because the permeability of these samples is in the Nadarcy level. The error rate meets the requirements of quantitative evaluation of true triaxial hydraulic fracturing fracture propagation. Figure 6 shows a different permeability on each face of the sample. The permeability of Face 2 of sample 1# is greater than those of the other four faces, and the homogeneities of the other four faces are better. The permeabilities of Faces 1, 4, and 5 of sample 2# are similar, and those of Faces 2 and 3 are similar. According to the permeability fluctuation and difference, the maximum difference of sample 1# is about 0.003 mD, and the maximum difference of sample 2# is about 0.004 mD. The permeability of the specimen increases exponentially after hydraulic fracturing. It can be seen that the permeability difference of this order of magnitude does not affect the description of hydraulic fracturing fracture propagation. In summary, it can be concluded that sample 1# has better homogeneity than sample 2#, which is more conducive to good comparison and evaluation of hydraulic fracturing fracture propagation.

4.2. After the Hydraulic Fracturing Experiment. *4.2.1. Experiment with new techniques.* After completing the hydraulic fracturing experiment, the conventional permeability test method and the established post-hydraulic fracturing permeability model were used to test and calculate the permeability of each face of the sample without removing, loading, and unloading true triaxial stress. The results are shown in Table 2. The permeability of some faces of sample 1# and 2# is greatly improved. It is found that the face without permeability does not produce fracturing fractures in later sample observations. In addition, the conventional testing methods cannot obtain the permeability of tight samples, and their testing accuracy cannot meet the requirements, so there is no permeability test result. Figure 7 shows permeability before and after hydraulic fracturing. It is found that the face permeability of artificial fractures generated by hydraulic fracturing increases by nearly 100,000 times, and the fracture permeability reaches the level of 100 mD. Two-phase gas−liquid can flow smoothly in the fracture, achieving a good fracturing effect. The permeability of Faces 1, 2, and 5 of sample 1# increases significantly. The permeability of Faces 1, 3, and 4 of sample 2# also increases significantly. They are consistent with the fracture propagation results observed in Figure 8. No fractures are found and no permeability is

https://doi.org/10.1021/acsomega.2c02517
ACS Omega 2022, 7, 27490−27502

Figure 8. Hydraulic fracturing fracture propagation: (a) Front view of sample 1#, (b) side view of sample 1#, (c) top view of sample 2#, and (d) side view of sample 2#.

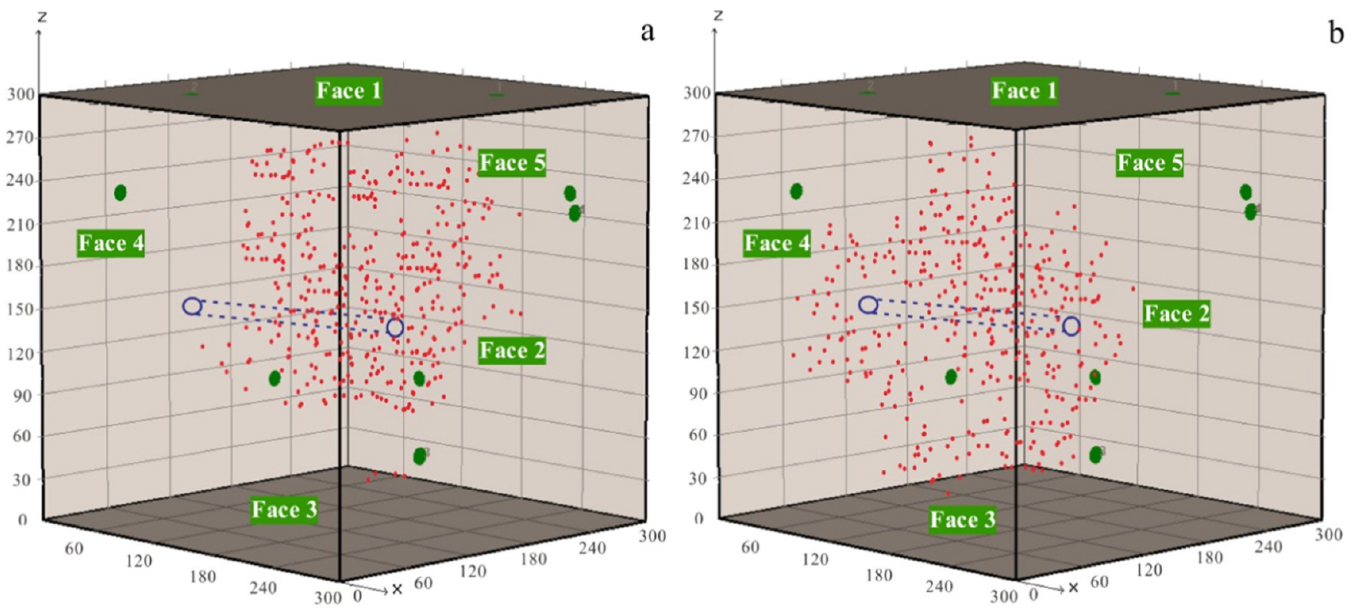

Figure 9. Hydraulic fracturing acoustic emission monitoring results: (a) sample 1# and (b) sample 2#.

obtained, which indicates that the experimental equipment and methods are reliable. It can be seen that this technology achieves the purpose of quantitatively evaluating the effect of crack propagation without changing the in situ true triaxial stress.

4.2.2. Experimental comparison. During the hydraulic fracturing experiment, acoustic emission is used to monitor the AE events caused by hydraulic fracturing. The permeability test results after hydraulic fracturing are analyzed combined with the appearance observation of fracture propagation of samples. Figures 8 and 9, respectively, show the monitoring and positioning of hydraulic fracturing fracture propagation and acoustic emission events. It is evident that the artificial cracks on Faces 1 and 5 of sample 1# have penetrated through the sample, which is consistent with the permeability test results. There are no apparent cracks on the other three faces. However, it is found from the monitoring results of AE events that a large number of acoustic emission events have occurred

https://doi.org/10.1021/acsomega.2c02517
ACS Omega 2022, 7, 27490−27502

in the direction of Face 2, which proves that there are a large number of rock fractures in this direction, and many microcracks are formed in the sample. These are consistent with the permeability test results listed in Table 2. AE events in the direction of Faces 3 and 4 are less, indicating that there are not a large number of cracks. The artificial fractures of Faces 1, 3, and 4 of sample 2# have penetrated through the sample. The permeability of these three faces has increased significantly. There are no obvious artificial cracks on Faces 2 and 5 of sample 2#. There is only one crack across Face 2 at the entrance of the experimental wellbore. Further observations show that the cracks do not penetrate through Face 2 and the cracks on the face are also wrapped by the core sleeve. So, Face 2 also has no permeability. This result agrees with the AE event monitoring results of sample 2# shown in Figure 9. AE events are mainly distributed in the directions of Faces 1, 3, and 4. These fracture propagation patterns match the magnitude and direction of the loading stress. Post-fracturing observation and AE event monitoring results further verify that the permeability variation in the in situ true triaxial environment can represent the cracks generated by the hydraulic fracturing of the sample. The accurate permeability is a means to quantitatively characterize the fracturing effect in all directions.

5. CONCLUSION

Based on the analysis of existing problems in the evaluation of the experimental results of true triaxial hydraulic fracturing, a new quantitative evaluation was proposed. A new experimental instrument was designed and fabricated. A matching experimental method was established. It carries out a comparative experiment. The results show that the new technique can quantitatively evaluate the fracture propagation effect of hydraulic fracturing, agreeing with small cylindrical samples, experimental observation, and AE results.

(1) It designed and fabricated a true triaxial stress loading and permeability integrated module and improved the sealing parts and structures of experimental specimens. It can carry out synchronously the hydraulic fracture propagation and permeability test under true triaxial stress.
(2) The new permeability test module was constructed. It realizes permeability measurement and data acquisition of a tight and large experimental specimen. Based on the developed instrument, models of different faces and the total permeability of the specimen were established under various states before and after hydraulic fracturing. It can obtain five faces and the total permeability of the specimen.
(3) Experimental results showed that the developed experimental instrument and method could achieve an excellent quantitative evaluation of true triaxial hydraulic fracturing experimental results. The test permeability error rate was within ±10%. Its error rate met the requirement of the assessment. Post-fracturing observation and AE event results further verified the permeability variation in the in situ true triaxial environment.

To sum up, we provide a new technique for quantitative evaluation of a true triaxial hydraulic fracturing fracture propagation experiment by developing a new experimental instrument and constructing new testing methods. It cannot directly obtain the permeability of tight specimens under the condition of a true triaxial fracture propagation experiment. It is helpful for a more refined assessment of fracture propagation. Due to the irregularity of the testing specimen, it is necessary to improve the edge seal to reduce the uncertainty risk.

■ ASSOCIATED CONTENT

Supporting Information

The Supporting Information is available free of charge at https://pubs.acs.org/doi/10.1021/acsomega.2c02517.

Schematic drawing of the specimen arrangement; plate groove; AE sensors and hole arrangement; permeability testing pipeline and joint; specimen core sleeve; wellbore design; gas booster module device; data acquisition and processing interface of the permeability test; specimen and wellbore distribution; specimen mold and specimen production; seal specimen; and specimen loaded (PDF)

■ AUTHOR INFORMATION

Corresponding Authors

Pei He − *National and Local Joint Engineering Research Center of Shale Gas Exploration and Development and Key Laboratory of Shale Gas Exploration, Ministry of Natural Resources, Chongqing Institute of Geology and Mineral Resources, Chongqing 400042, China*; orcid.org/0000-0003-3694-433X; Email: hepei131180@163.com

Zhaohui Lu − *National and Local Joint Engineering Research Center of Shale Gas Exploration and Development and Key Laboratory of Shale Gas Exploration, Ministry of Natural Resources, Chongqing Institute of Geology and Mineral Resources, Chongqing 400042, China*; Email: luzhaohui929@126.com

Authors

Linhua Pan − *Sinopec Exploration & Production Research Institute, Beijing 100083, China*

Jiankun Zhou − *National and Local Joint Engineering Research Center of Shale Gas Exploration and Development, Chongqing Institute of Geology and Mineral Resources, Chongqing 400042, China*

Chun Meng − *National and Local Joint Engineering Research Center of Shale Gas Exploration and Development, Chongqing Institute of Geology and Mineral Resources, Chongqing 400042, China*

Huawen Yu − *National and Local Joint Engineering Research Center of Shale Gas Exploration and Development, Chongqing Institute of Geology and Mineral Resources, Chongqing 400042, China*

Complete contact information is available at: https://pubs.acs.org/10.1021/acsomega.2c02517

Notes

The authors declare no competing financial interest.

■ ACKNOWLEDGMENTS

This work was sponsored by the National Natural Science Foundation of China (No. 52004047), the Natural Science Foundation of Chongqing, China (Nos. cstc2020jcyj-msxmX0610 and cstc2020jcyj-msxmX1027), and Special Project for Performance Incentive and Guidance of Chongqing

https://doi.org/10.1021/acsomega.2c02517
ACS Omega 2022, 7, 27490−27502

Research Institutions (Nos. cstc2021jxjl90004, cstc2021jxjl20024, cstc2020jxjl90001, and cstc2021jxjl20014).

REFERENCES

(1) Soeder, D. J. The successful development of gas and oil resources from shales in North America. *J. Pet. Sci. Eng.* **2018**, *163*, 399−420.
(2) Ivanova, N. O.; Xu, Z.; Liu, Q.; Masliyah, J. H. Surface forces in unconventional oil processing. *Curr. Opin. Colloid Interface Sci.* **2017**, *27*, 63−73.
(3) Li, F.; Yuan, Q.; Li, T.; Li, Z.; Sun, C.; Chen, G. A review: Enhanced recovery of natural gas hydrate reservoirs. *Chin. J. Chem. Eng.* **2019**, *27*, 2062−2073.
(4) Shen, A.; Liu, Y.; Wang, X.; Cai, B.; He, C.; Liang, S. The geological characteristics and exploration of continental tight oil: an investigation in China. *J. Pet. Explor. Prod. Technol.* **2019**, *9*, 1651−1658.
(5) He, P.; Xiong, J.; Lu, Z.; Pan, L.; Qin, D. Study of pulse wave propagation and attenuation mechanism in shale reservoirs during pulse hydraulic fracturing. *Arabian J. Sci. Eng.* **2018**, *43*, 6509−6522.
(6) Tariq, Z.; Mahmoud, M.; Alade, O.; Abdulraheem, A.; Mustafa, A.; Mokheimer, E.; Al-Jawad, M.; Al-Nakhli, A. Productivity Enhancement in Multilayered Unconventional Rocks Using Thermo-chemicals. *J. Energy Resour. Technol.* **2021**, *143*, No. 033001.
(7) Cheng, Y.; Zhang, Y.; Yu, Z.; Hu, Z.; Ma, Y.; Yang, Y. Experimental and numerical studies on hydraulic fracturing characteristics with different injection flow rates in granite geothermal reservoir. *Energy Sci. Eng.* **2021**, *9*, 142−168.
(8) Liu, Y.; Xu, T.; Yuan, Y.; Feng, B.; Tang, X.; Liu, X.; Cui, Z. A laboratory study on fracture initiation and propagation of granite under cyclic-injection hydraulic fracturing. *J. Pet. Sci. Eng.* **2022**, *212*, No. 110278.
(9) Zhang, X.; Lu, Y.; Tang, J.; Zhou, Z.; Liao, Y. Experimental study on fracture initiation and propagation in shale using supercritical carbon dioxide fracturing. *Fuel* **2017**, *190*, 370−378.
(10) Tariq, Z.; Mahmoud, M.; Abdulraheem, A.; Al-Shehri, D.; Murtaza, M. An environment friendly approach to reduce the breakdown pressure of high strength unconventional rocks by cyclic hydraulic fracturing. *J. Energy Resour. Technol.* **2020**, *142*, No. 043002.
(11) Tariq, Z.; Alijewad, M. S.; Murtaza, M.; Mahmoud, M.; Al-Shehri, D.; Abdulraheem, A. *A Data-Driven Approach to Predict the Breakdown Pressure of the Tight and Unconventional Formation*, Paper presented at the SPE Annual Technical Conference and Exhibition,-Dubai, UAE, 2021.
(12) Wang, K.; Liu, H.; Luo, J.; Wu, K.; Chen, Z. A comprehensive model coupling embedded discrete fractures, multiple interacting continua, and geomechanics in shale gas reservoirs with multiscale fractures. *Energy Fuels* **2017**, *31*, 7758−7776.
(13) Shen, Z.; Zhou, L.; Li, H.; Lu, Z.; Cai, J. Experimental and numerical study on the anisotropic and nonlinear gas flow behavior of a single coal fracture under loading. *Energy Fuels* **2020**, *34*, 4230−4242.
(14) Wang, R.; Pan, J.; Wang, Z.; Li, G.; Ge, T.; Zheng, H.; Wang, X. Influence of in situ stress on well test permeability and hydraulic fracturing of the Fanzhuang Block, Qinshui Basin. *Energy Fuels* **2021**, *35*, 2121−2133.
(15) Li, X.; Wu, Z.; Takahashi, M.; YASUHARA, K. Permeability anisotropy of shirahama sandstone under true triaxial stresses. *Doboku Gakkai Ronbunshu* **2002**, *2002*, 1−11.
(16) Liu, Y.; Yin, G.; Zhang, D.; Li, M.; Deng, B.; Liu, C.; Zhao, H.; Yin, S. Directional permeability evolution in intact and fractured coal subjected to true-triaxial stresses under dry and water-saturated conditions. *Int. J. Rock Mech. Min. Sci.* **2019**, *119*, 22−34.
(17) Sato, M.; Takemura, T.; Takahashi, M. Development of the permeability anisotropy of submarine sedimentary rocks under true triaxial stresses. *Int. J. Rock Mech. Min. Sci.* **2018**, *108*, 118−127.
(18) King, M. S. Elastic wave propagation in and permeability for rocks with multiple parallel fractures. *Int. J. Rock Mech. Min. Sci.* **2002**, *39*, 1033−1043.
(19) Liu, Q.; Cheng, Y.; Haifeng, W.; Hongxing, Z.; Liang, W.; Wei, L.; Hongyong, L. Numerical assessment of the effect of equilibration time on coal permeability evolution characteristics. *Fuel* **2015**, *140*, 81−89.
(20) Li, M.; Yin, G.; Xu, J.; Li, W.; Song, Z.; Jiang, C. A novel true triaxial apparatus to study the geomechanical and fluid flow aspects of energy exploitations in geological formations. *Rock Mech. Rock Eng.* **2016**, *49*, 4647−4659.
(21) Li, M.; Yin, G.; Xu, J.; Cao, J.; Song, Z. Permeability evolution of shale under anisotropic true triaxial stress conditions. *Int. J. Coal Geol.* **2016**, *165*, 142−148.
(22) Jiang, T.; Yao, W.; Sun, X.; Qi, C.; Li, X.; Xia, K.; Zhang, J.; Nasseri, M. H. B. Evolution of anisotropic permeability of fractured sandstones subjected to true-triaxial stresses during reservoir depletion. *J. Pet. Sci. Eng.* **2021**, *200*, No. 108251.
(23) Feng, X. T.; Zhang, X.; Kong, R.; Wang, G. A novel Mogi type true triaxial testing apparatus and its use to obtain complete stress−strain curves of hard rocks. *Rock Mech. Rock Eng.* **2016**, *49*, 1649−1662.
(24) Frash, L. P.; Gutierrez, M.; Hampton, J. True-triaxial apparatus for simulation of hydraulically fractured multi-borehole hot dry rock reservoirs. *Int. J. Rock Mech. Min. Sci.* **2014**, *70*, 496−506.
(25) Huang, B.; Li, P. Experimental investigation on the basic law of the fracture spatial morphology for water pressure blasting in a drillhole under true triaxial stress. *Rock Mech. Rock Eng.* **2015**, *48*, 1699−1709.
(26) Shi, J. Q.; Durucan, S. Drawdown induced changes in permeability of coalbeds: a new interpretation of the reservoir response to primary recovery. *Transp. Porous Media* **2004**, *56*, 1−16.
(27) Shi, J. Q.; Durucan, S. A model for changes in coalbed permeability during primary and enhanced methane recovery. *SPE Reservoir Eval. Eng.* **2005**, *8*, 291−299.
(28) Seidle, J. R.; Huitt, L. G. In *Experimental Measurement of Coal Matrix Shrinkage Due to Gas Desorption and Implications for Cleat Permeability Increases*, International meeting on petroleum Engineering; OnePetro, 1995.
(29) Connell, L. D.; Lu, M.; Pan, Z. An analytical coal permeability model for tri-axial strain and stress conditions. *Int. J. Coal Geol.* **2010**, *84*, 103−114.
(30) Lyu, Q.; Shi, J.; Gamage, R. P. Effects of testing method, lithology and fluid-rock interactions on shale permeability: a review of laboratory measurements. *J. Nat. Gas Sci. Eng.* **2020**, *78*, No. 103302.
(31) Sander, R.; Pan, Z.; Connell, L. D. Laboratory measurement of low permeability unconventional gas reservoir rocks: A review of experimental methods. *J. Nat. Gas Sci. Eng.* **2017**, *37*, 248−279.
(32) Zhao, X.; Sang, Q.; Li, Y.; Liu, H.; Li, Z.; Liu, Y.; Dong, M. Dynamic effective permeability of a laminated structure with cross flow in the transient flow process and its application to reservoir simulation. *J. Pet. Sci. Eng.* **2022**, *208*, No. 109649.
(33) Tokareva, M. A. Solvability of initial boundary value problem for the equations of filtration in poroelastic media. *J. Phys.: Conf. Ser.* **2016**, *722*, No. 012037.
(34) Shi, J.; Sun, Z.; Wu, K.; Wang, K.; Huang, L.; Liu, W.; Li, X. Effect of pore shape on nanoconfined gas flow behavior: Implication for characterizing permeability of realistic shale matrix. *Ind. Eng. Chem. Res.* **2019**, *58*, 8835−8846.
(35) Yu, P.; Liu, Y.; Wang, J.; Kong, C.; Gu, W.; Xue, L.; Cheng, Z.; Jiang, L. A new fracture permeability model: Influence of surrounding rocks and matrix pressure. *J. Pet. Sci. Eng.* **2020**, *193*, No. 107320.
(36) Mayeli, P.; Sheard, G. J. Buoyancy-driven flows beyond the Boussinesq approximation: A brief review. *Int. Commun. Heat Mass Transfer* **2021**, *125*, No. 105316.

https://doi.org/10.1021/acsomega.2c02517
ACS Omega 2022, 7, 27490−27502